

pubs.acs.org/JPCL Letter

# Activated Lone-Pair Electrons Lead to Low Lattice Thermal Conductivity: A Case Study of Boron Arsenide

Guangzhao Qin,\* Jianhua Xu, Huimin Wang,\* Zhenzhen Qin,\* and Ming Hu\*



Cite This: J. Phys. Chem. Lett. 2023, 14, 139–147



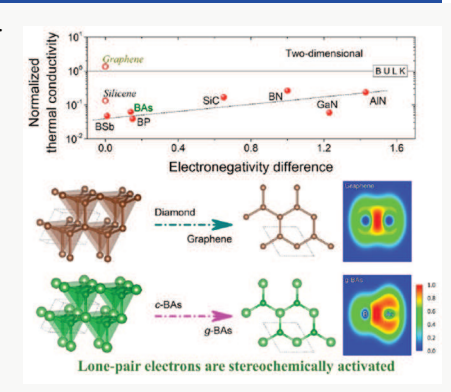
**ACCESS** I

III Metrics & More

Article Recommendations

Supporting Information

**ABSTRACT:** Reducing thermal conductivity ( $\kappa$ ) is of great significance to lots of applications, such as thermal insulation, thermoelectrics, etc. In this study, we propose an effective approach for realizing low  $\kappa$  by introducing lone-pair electrons or making the lone-pair electrons stereochemically active through bond nanodesigning. By cutting at the (111) cross section of the three-dimensional cubic boron arsenide (c-BAs), the  $\kappa$  is lowered by more than 1 order of magnitude in the resultant two-dimensional graphene-like BAs (g-BAs). The underlying mechanism of activating lone-pair electrons is analyzed based on the comparative study on the thermal transport properties and electronic structures of g-BAs, c-BAs, graphene, and diamond (c-BAs  $\rightarrow g$ -BAs vs diamond  $\rightarrow$  graphene). The proposed approach for realizing low  $\kappa$  and the underlying mechanism uncovered in this study would largely benefit the design of advanced thermal functional materials, especially in future research involving novel materials for energy applications.



ue to the ability of firsthand solid-state conversion to electrical power from thermal energy, especially for waste heat reusing, thermoelectrics have attracted a lot of attention in recent years. Thermoelectrics have lots of valuable applications in recovering resources and thus may make crucial contributions to the crisis of the environment by solving energy problems. Moreover, thermoelectrics possess the advantages of having no moving components and being environmentally friendly compared to traditional mechanical heat engines. Generally, the thermoelectric efficiency and performance can be characterized by a dimensionless figure of merits.

$$ZT = S^2 \sigma T / \kappa \tag{1}$$

where S,  $\sigma$ , T, and  $\kappa$  are the thermopower (Seebeck coefficient), electrical conductivity, absolute temperature, and total thermal conductivity, respectively. The commercial applications in the industry of thermoelectric devices are currently limited by the low ZT merit. To approach the Carnot coefficient as closely as possible, a high energy generation efficiency is necessary, which corresponds to a large ZT merit. Based on the definition (eq 1), lowering the  $\kappa$  would be more efficient to boost the ZT merit due to the inversely proportional relation.<sup>4</sup>

Lots of potential high ZT materials have limited applications in the thermoelectric field because of high  $\kappa$ , which makes it highly urgent to find an effective approach to lower the intrinsic  $\kappa$ . It has been reported that the cubic boron arsenide (c-BAs) has attracted wide attention in electronics, photoelectrics, water decomposition, etc., because the c-BAs is a revolutionary semiconductor with high ambipolar mobilities

combined with the ultrahigh thermal conductivity.<sup>5</sup> Previous theoretical studies predicted that cubic boron arsenide (c-BAs) in the bulk form has an exceptionally high  $\kappa$  over 2000 W/mK, which is comparable to the bulk carbon crystals (diamond) with record highest  $\kappa$ . The ultrahigh  $\kappa$  of c-BAs was analyzed to be resulted from the large phonon band gap between acoustic and optical phonon branches together with the bunching of the acoustic phonon branches, which reduce phonon-phonon scattering.6 The features of the phonon dispersion of c-BAs analyzed based on first-principles calculations are then confirmed by experimental measurements based on inelastic X-ray scattering. By considering the phonon-phonon scattering involving four phonons, Feng et al. found that the  $\kappa$  of c-BAs reduces from 2200 to 1400 W/ mK, which was recently confirmed by experimental studies.  $^{9-11}$  Experimental measurements reveal that the  $\kappa$  of BAs can be suppressed by the arsenic deficiency or vacancy in the BAs sample 12 and the phonon boundary scattering in BAs microstructures. <sup>13,14</sup> However, the obtained  $\kappa$  of BAs is still too high, which limits its potential applications in thermoelectrics, despite that the Seebeck coefficient and thermoelectric power factor of BAs are comparable to those of bismuth telluride, 14 which is one of the most commonly used thermoelectric materials. Thus, it would be meaningful if one can find an

Received: October 27, 2022 Accepted: December 22, 2022



effective approach to lower the intrinsic  $\kappa$  of BAs to benefit its applications in thermoelectrics. Moreover, the approach that makes such a high  $\kappa$  material applicable for thermoelectrics would also largely benefit the design of thermoelectric devices with improved performance by lowering  $\kappa$ , especially in the future research involving novel materials for energy application.

With the rise of graphene, people have shown great enthusiasm for investigating two-dimensional (2D) materials. As an emerging 2D material, single-layer boron arsenide with a plane honeycomb structure similar to graphene (*g*-BAs), which has been proved to be stable in the calculations, shows many excellent properties, such as high carrier mobility<sup>15</sup> and piezoelectric coefficient, high Seebeck coefficient and power factor, and suitable band gap matching well with tandem solar cell materials. These studies proclaimed that *g*-BAs is a prospective material in broad fields such as piezoelectrics, thermoelectrics, photoelectrics, etc., that would make it worth further study. In addition, researchers have made an effort to explore various properties of *g*-BAs, including doping, heterojunction, heterojunction, electric field regulation, strain engineering, tec.

With the significant role of thermal transport in the application fields, such as in computation clusters, high-energy batteries, nuclear reactors, laser weapons, etc., it is necessary to pay attention to the heat transfer performance of g-BAs, and researchers have carried out lots of fundamental researches.<sup>24,25</sup> For instance, a recent study has predicted the thermal conductivity of g-BAs to be about 181 W/mK.<sup>26</sup> Although it is higher than that of most 2D semiconductor materials, such as g-BP and g-GaN,<sup>27</sup> the thermal conductivity of g-BAs is still far lower than that of graphene with a similar honeycomb structure and the corresponding cubic structure, which aroused great attention. Compared with graphene with the same planar honeycomb structure, it arouses a problem: Why is the thermal conductivity of g-BAs far lower than that of its cubic structure and graphene? Researchers have tried to establish a physical model that explains the thermal transport in 2D materials. Some scholars believed that the ZO branch of g-BAs provides more scattering channels and the weakening of the phonon bunching effect caused by secondary scattering introduces greater thermal resistance, resulting in its low thermal conductivity.<sup>25</sup> However, it is still hard to fully explain this abnormal physical phenomenon and its electronic origin. Thus, exploring the mechanisms and the electronic origin behind the abnormally low thermal conductivity of g-BAs will not only promote the probability of its application in thermoelectric devices but also help us to better understand the physical foundation of phonon thermal transport. This study could provide practical means of micro/nanoscale design to modulate thermal transport behaviors for thermoelectric applications and further promote the 2D materials from theory to application.

In this work, by choosing the typical 2D materials (graphene, silicene, BN, AlN, GaN, BP, BAs, BSb, and SiC) as representatives, we propose an effective approach for realizing low  $\kappa$  by bond nanodesigning to make the lone-pair electrons stereochemically active. As a result, a much lower  $\kappa$  can be generally achieved by solving the phonon Boltzmann transport equation (BTE) based on first-principles calculations, except the case of graphene (Figure 1 and Figure S5). As a specific case study, when transforming the three-dimensional (3D) c-BAs into the 2D graphene-like BAs (g-BAs), the  $\kappa$  is

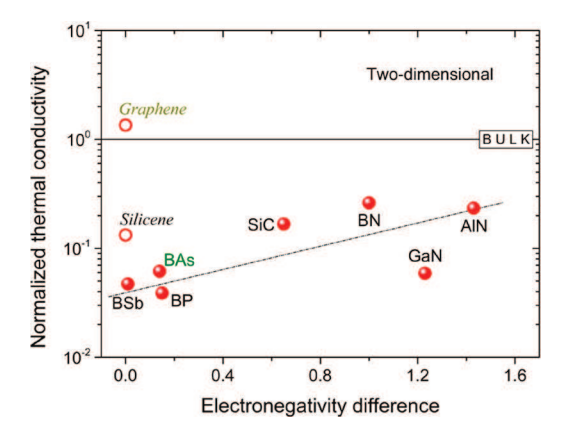


**Figure 1.** Thermal conductivity of typical 2D materials (graphene, silicene, BN, AlN, GaN, BP, BAs, BSb, and SiC) at 300 K, which are normalized to the bulk counterparts, respectively. The 2D materials possess a lower  $\kappa$  compared to the bulk counterparts, except graphene. The dotted line is for an eye guide. The specific data can be found in Table S1.

found to be lowered by more than 1 order of magnitude (Figure 2) due to the stereochemically activated lone-pair electrons. The underlying mechanism is analyzed based on the comparative study on the thermal transport properties of *g*-BAs, *c*-BAs, graphene, and diamond, considering the similarity of the transformation from 3D cubic to 2D honeycomb planar geometry structures (c-BAs  $\rightarrow g$ -BAs vs diamond  $\rightarrow$  graphene) but the opposite trend for the  $\kappa$  modulation. Moreover, deep

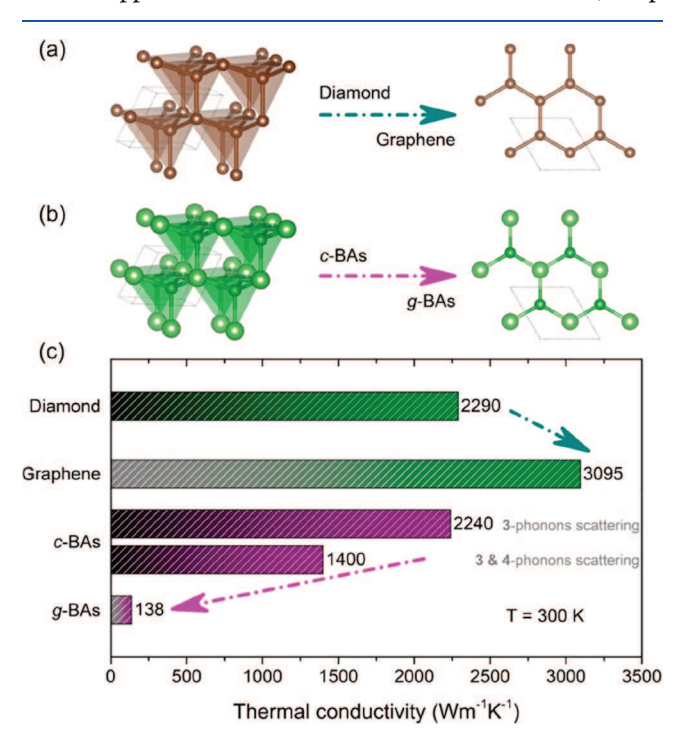


**Figure 2.** The similarity of the transformation from 3D cubic to 2D honeycomb planar geometry structures (*c*-BAs  $\rightarrow$  *g*-BAs vs diamond  $\rightarrow$  graphene) is in contrast to the opposite  $\kappa$  variation. When transforming from 3D into 2D, the  $\kappa$  of BAs is found to be anomalously lowered by more than 1 order of magnitude. (a) The structure of graphene in 2D is the (111) cross section of the structure of diamond in 3D, which is planar due to the sp<sup>2</sup> hybridization of carbon atoms. (b) The *g*-BAs to *c*-BAs is like graphene to diamond. (c) The comparison of  $\kappa$  of diamond, graphene, *c*-BAs, <sup>6,8</sup> and *g*-BAs.

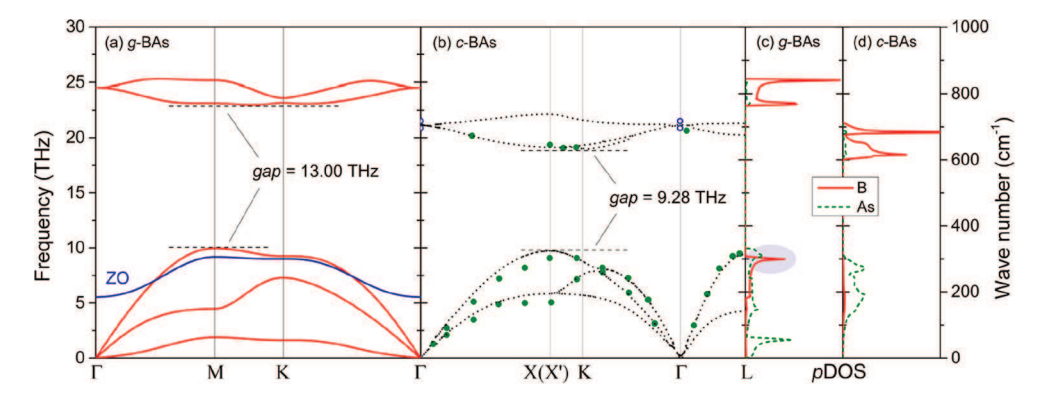


Figure 3. Comparison of the phonon dispersion of boron arsenide in 2D (g-BAs) and 3D (c-BAs). (a) The phonon dispersion of g-BAs along the high-symmetry points, where the out-pf-plane flexural acoustic (FA) phonon branch shows a good quadratic behavior (Figure S1). There exists a huge gap of 13.00 THz between the optical and acoustic phonon branches. The z-direction optical (ZO) phonon branch, which is below the gap, is highlighted in blue. (b) The phonon dispersion of c-BAs along the high-symmetry points, where dotted lines in black are from theoretical calculations and blue/green points are from experimental measurements. The gap between the optical and acoustic phonon branches is 9.28 THz. (c, d) The partial density of states (pDOS) of (c) g-BAs and (d) c-BAs, where the contribution from boron (B) atoms to ZO is highlighted with a colored ellipse.

insight into the electronic origin is gained by performing fundamental analysis on the electronic structures. Most importantly, a strong correlation between  $\kappa$  modulation and electronegativity difference for g-BAs is well established in this work, where the mechanism can be further extended to more systems (not limited to group III—V compounds) with similar lone-pair electrons.

By cutting the 3D cubic structure of c-BAs at the (111) cross section, g-BAs can be obtained with a similar planar honeycomb structure as graphene (c-BAs  $\rightarrow g$ -BAs vs diamond  $\rightarrow$  graphene). The  $\kappa$  of g-BAs is obtained to be 137.70 W/mK, which is more than 1 order of magnitude lower than that of graphene (3094.98 W/mK). Note that only three-phonon scattering is considered here for simplicity. The  $\kappa$  of g-BAs could be further lowered if four-phonon scattering is included. The in-plane longitudinal acoustic (LA), transverse acoustic (TA), and out-of-plane flexural acoustic (FA) phonon branches contribute 28.5%, 43.1%, and 26.9%, respectively. The  $\kappa$  values of g-BAs are 89.3 and 137.7 W/mK before and after iteration, respectively. The large difference in the RTA and iteration results means that the proportion of N-process could be large and there exists strong phonon hydrodynamics in g-BAs.

The lower  $\kappa$  of g-BAs than that of graphene is very intriguing considering the similarity of their planar honeycomb geometry structures (Figure 2a,b). In particular, the  $\kappa$  of c-BAs is comparable to diamond (Figure 2c),6 both of which share the same cubic structures and are the 3D counterparts of g-BAs and graphene, respectively (Figure 2a,b). However, when transforming from 3D to 2D, a huge difference emerges that the  $\kappa$  of g-BAs (the 2D counterpart of c-BAs) is much lower than that of graphene (the 2D counterpart of diamond), despite the comparable  $\kappa$  of c-BAs and diamond (Figure 2c). In the following, we perform a detailed analysis to achieve a fundamental understanding on the anomalously lowered  $\kappa$  of g-BAs compared to c-BAs, diamond, and graphene. With the uncovered underlying mechanism, the generally lower  $\kappa$  of 2D systems than that of the 3D form as shown in Figure 1 and Figure S5 can also be well understood.

Figure 3a shows the phonon dispersion of g-BAs, in comparison with c-BAs (Figure 3b). It was claimed in a previous study<sup>6</sup> that the ultrahigh  $\kappa$  of c-BAs comparable to diamond results from the large phonon band gap between

acoustic and optical phonon branches together with the bunching of the acoustic phonon branches. The features of the phonon dispersion of c-BAs analyzed based on first-principles calculations are then confirmed by experimental measurements based on inelastic X-ray scattering,<sup>7</sup> as reproduced in Figure 3b. When transforming from 3D c-BAs to 2D g-BAs, the phonon dispersions show some different features, which could have a remarkable effect on the  $\kappa$ . (i) The phonon band gap in g-BAs is 13.00 THz, which is larger than that in c-BAs (9.28 THz). The larger phonon band gap is expected to not have a negative effect on the  $\kappa$  for the three-phonon scattering processes considered here. (ii) The z-direction optical (ZO) phonon branch in g-BAs is below the bandgap, as highlighted in Figure 3a, which could lead to more scattering probability by coupling with acoustic phonon branches (especially LA). See Note S2 and Figure S2 for more information on the coupling, as revealed by phonon-phonon scattering channels. Such coupling is absent in the 3D c-BAs. (iii) The bunching of acoustic phonon branches in g-BAs becomes weak due to the separation of the three phonon branches. The weakened bunching effect for acoustic phonon branches together with the coupling with the ZO phonon branch could lead to more phonon-phonon scattering, and thus is probably responsible for the anomalously lower  $\kappa$  of g-BAs than that of c-BAs.

The ZO phonon branch in g-BAs is mainly contributed from the boron (B) atoms, as revealed by the partial density of states (pDOS) in Figure 3c. In fact, due to the mass difference, the optical phonon branches in both c-BAs and g-BAs are contributed from the B atoms (Figure 3c,d). With the geometry structures transformed from 3D (c-BAs) to 2D (g-BAs), the z-direction vibration of B atoms is totally different due to the 2D nature of bondings and structural symmetry, which lowers the frequency of ZO and provides more scattering probability in g-BAs by strongly coupling with acoustic phonon branches (Figure 3a) (Note S2 and Figure S2). Such a phenomenon is also observed in monolayer GaN.<sup>27,29</sup> Due to the 2D nature of the g-BAs, the ZA shows quadratic behavior. Thus, more low-frequency phonons exist in g-BAs compared to the c-BAs, as revealed by the pDOS (Figure 3c,d).

All the possible phonon-phonon scattering events quantified by the scattering phase space are determined based on the

phonon dispersions by conserving both energy and crystal momentum with symmetry included 30-33

$$\omega_{j}(\vec{q}) \pm \omega_{j'}(\vec{q'}) = \omega_{j''}(\vec{q''})$$

$$\vec{q} \pm \vec{q'} = \vec{q''} + \vec{K}$$
(2)

where  $\omega$  is the frequency of phonon modes ( $\hbar\omega$  is the corresponding energy) and  $\vec{q}$  is the wave vector. The normal process corresponds to  $\vec{K}=0$ , while the Umklapp process corresponds to  $\vec{K}\neq 0$ . Figure 4 presents the phase space of

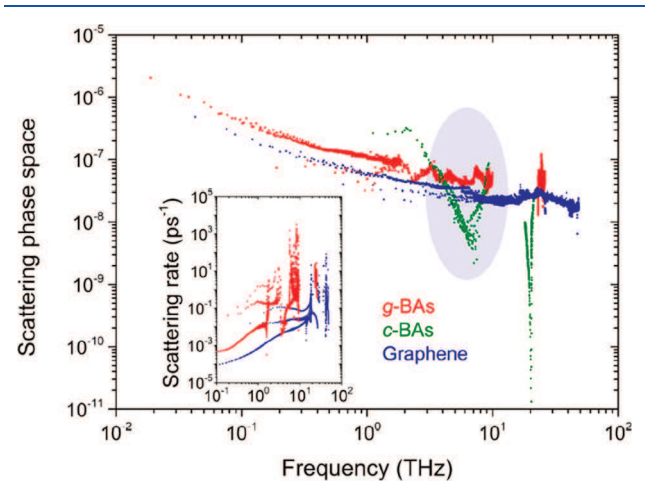


**Figure 4.** Comparison of the phonon—phonon scattering phase space of *g*-BAs with *c*-BAs and graphene. The colored ellipse highlights the larger scattering phase space of *g*-BAs than that of *c*-BAs in the frequency range of 5–10 THz, where the ZO phonon branch lies. (Inset) The comparison of the scattering rate between *g*-BAs and graphene.

three-phonon scattering in g-BAs, in comparison with that in c-BAs. The scattering phase space in c-BAs is small due to the large acoustic-optical phonon band gap, which is responsible for the ultrahigh  $\kappa$  of c-BAs as analyzed in a previous study. However, the scattering phase space in g-BAs is larger than that in c-BAs, especially for the frequency range of s-10 THz (Figure 4), despite the larger gap in g-BAs than that in c-BAs

(Figure 3a,b). The enhanced scattering probability could be attributed to the weakened bunching effect for acoustic phonon branches together with their coupling with the ZO phonon branch in g-BAs (Figure 3a), which partially explains the anomalously lower  $\kappa$  of g-BAs than that of c-BAs.

By comparing the phase spaces between g-BAs and graphene, we also found that the overall scattering phase space in g-BAs is larger than that in graphene. Thus, the anomalously lower  $\kappa$  of g-BAs than that of graphene is understandable despite their similar structures. However, it should be noted that the difference in the scattering phase space is much less than 1 order of magnitude, which cannot fully explain the large difference in the scattering rate (inset of Figure 4) and further the more than 1 order of magnitude lower  $\kappa$  of g-BAs (137.70 W/mK) than graphene (3094.98 W/mK). Therefore, there should be some other mechanism also responsible for the anomalously low  $\kappa$  of g-BAs beyond the scattering phase space and the phonon group velocity.

It is well-known that the phonon lifetime is governed by two factors: phonon—phonon scattering phase space and strength. The phonon—phonon scattering strength describes the strength of the phonon—phonon scattering process, which is governed by the anharmonic nature of the system. The Grüneisen parameter that describes the phonon anharmonicity can be calculated based on the change of phonon frequency with respect to the volume change

$$\gamma = -\frac{V}{\omega} \frac{\partial \omega}{\partial V} \tag{3}$$

Figure 5a shows the obtained Grüneisen parameter of g-BAs, in comparison with graphene. The FA phonon branch possesses the largest magnitude of the Grüneisen parameter for both g-BAs and graphene, and the magnitude is larger in g-BAs than in graphene, revealing the stronger phonon anharmonicity in g-BAs. Thus, the more than 1 order of magnitude lower  $\kappa$  of g-BAs than that of graphene can be well understood by combining the larger scattering phase space (Figure 4) and the stronger phonon anharmonicity in g-BAs.

The phonon anharmonicity can also be intuitively revealed by the potential energy well. To have an explicit look at the anharmonicity, the potential energy wells (potential energy changes per atom due to the atomic displacement) of g-BAs

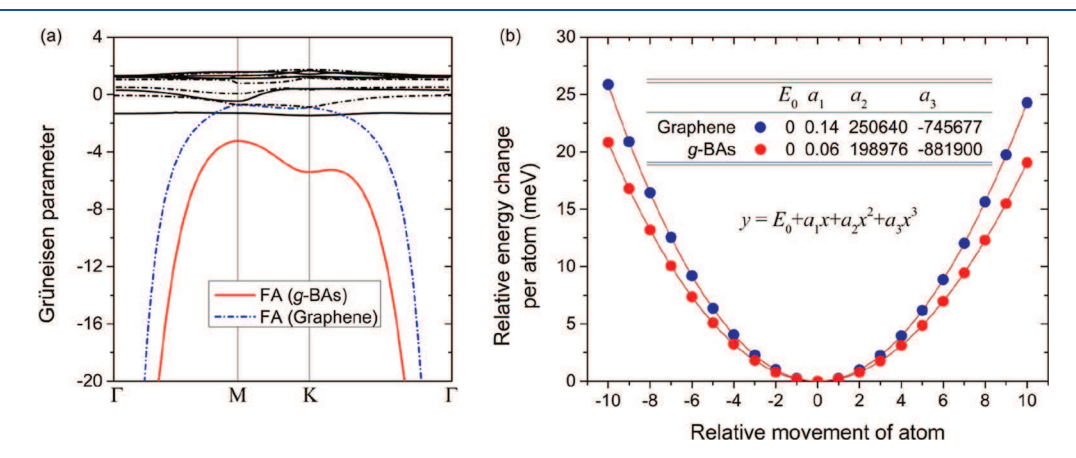


**Figure 5.** Strong phonon anharmonicity in g-BAs. (a) Comparison of Grüneisen parameters between g-BAs and graphene. The colored lines highlight the Grüneisen parameters of the FA phonon branch. (b) Comparison of potential energy wells between g-BAs and graphene. The atom is moved along the bonding direction. Points are from first-principles calculations, and lines are fittings to the formula shown on site. Inset table: The fitted parameters for g-BAs and graphene, respectively.

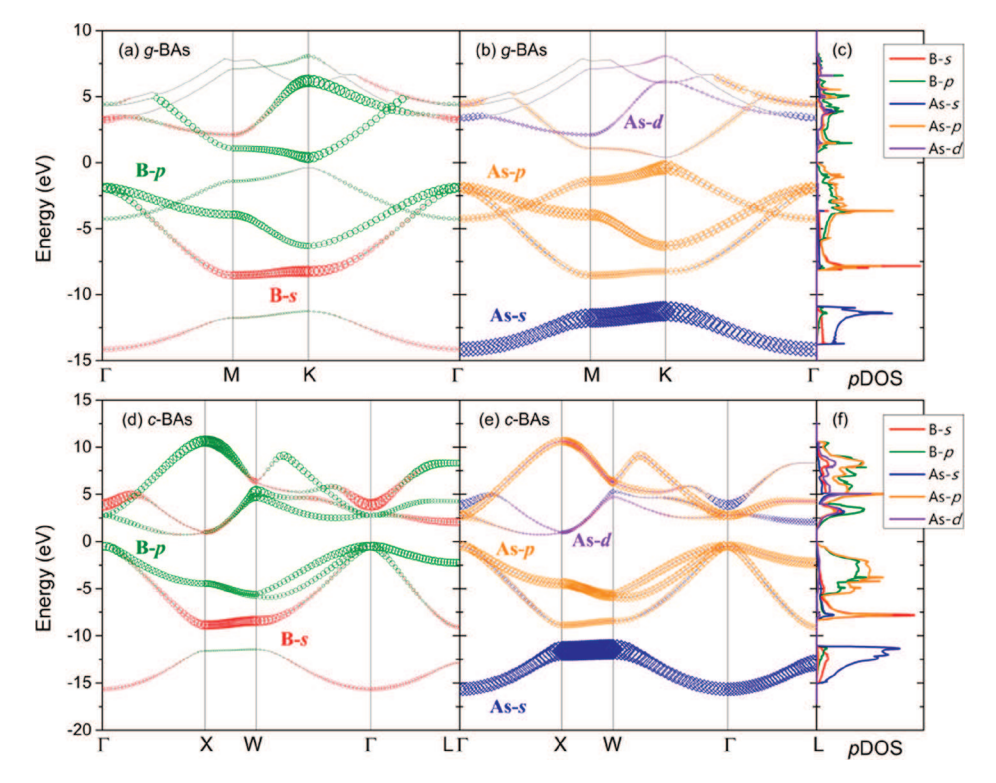


Figure 6. Orbital projected electronic structures, revealing the nonbonding lone-pair As-s electrons. (a-c) The orbital projected (a, b) electronic band structures and (c) density of states (DOS) for g-BAs. The electronic structures are projected to (a) B-s/p and (b) As-s/p/d orbitals. (d-f) Similar figures for c-BAs in comparison.

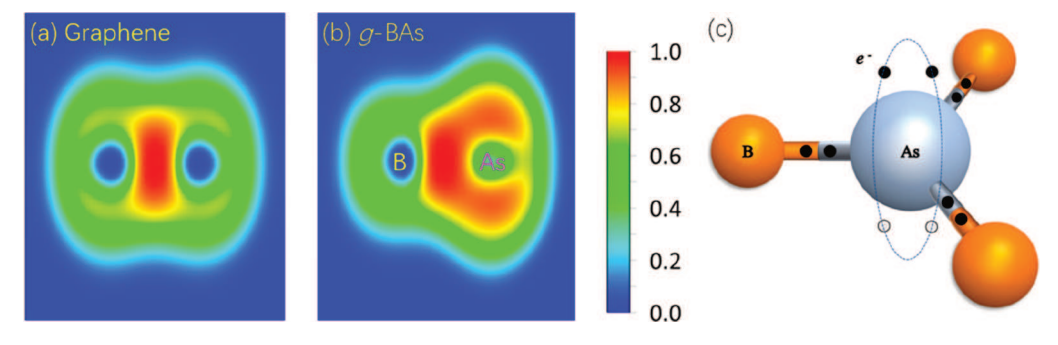


Figure 7. Side views of the electron localization function (ELF) for (a) graphene and (b) g-BAs. The comparison reveals the stereochemically activated lone-pair electrons in g-BAs, which are nonbonding around arsenide (As) atom. (c) Schematic diagram of lone-pair electrons in g-BAs.

and graphene are plotted in Figure 5b for comparison. Both potential wells are asymmetric with respect to the positive and negative atomic displacements, indicating the asymmetry in the ability of an atom vibrating around its equilibrium position and the nonlinear dependence of restoring forces on atomic displacement amplitudes, which is the direct evidence of the anharmonicity. We further fit the calculated points for g-BAs and graphene, respectively, with the polynomial

$$y = E_0 + a_1 x + a_2 x^2 + a_3 x^3 (4)$$

where y is the relative energy change per atom and x is the relative movement of atom. The fitted parameters for g-BAs and graphene are listed in the table as an inset in Figure 5b. The fitted  $a_1$  term means the force needed to move atoms. The fitted quadric  $(a_2)$  and cubic  $(a_3)$  terms correspond to the harmonicity and anharmonicity, respectively. The relatively smaller harmonic term in g-BAs reveals the weaker bonding strength of the B-As bond than that of the C-C bond in graphene, and the relatively larger magnitude of the

anharmonic term reveals stronger phonon anharmonicity in g-BAs.

To gain deep insight into the origin of the strong phonon anharmonicity in *g*-BAs, we further perform fundamental analysis on the electronic structures to uncover the underlying mechanism. We will show that the strong phonon anharmonicity in *g*-BAs is fundamentally driven by the stereochemically activated lone-pair electrons due to the special orbital hybridization.

The orbital projected electronic structures [band structure and density of states (DOS)] of g-BAs are depicted in Figure 6a-c. A direct band gap ( $\sim$ 0.75 eV) emerges in g-BAs, which is different from the indirect band gap in c-BAs (Figure 6d,e). As shown in Figure 6a-c, the bonding states in g-BAs are governed by the B-s/p and As-p orbitals. As for B atom, all three valence electrons are involved in the formation of B-As  $\sigma$  bonds due to the sp<sup>2</sup>-hybridization (Figure 6a). The situation is totally different for the As atom which possesses five valence electrons. The As-s orbital is largely ( $\sim$ 10 eV) confined below

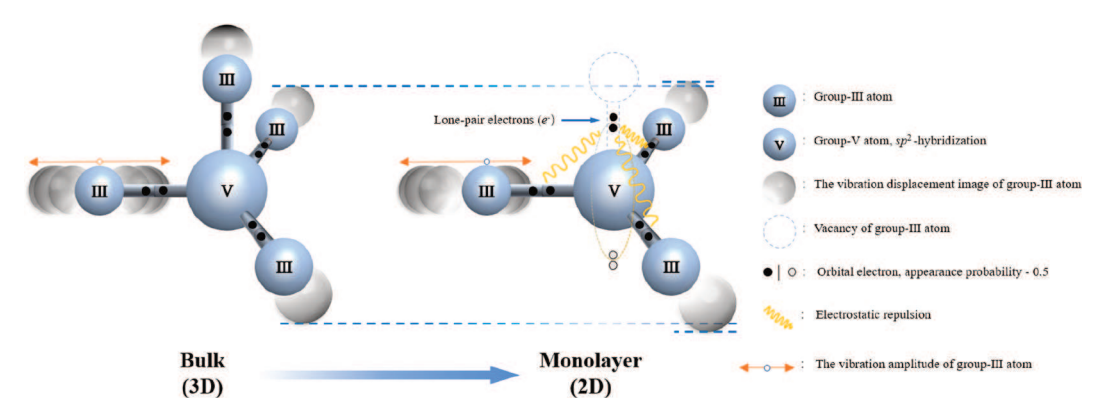


Figure 8. Schematics of the lone-pair electrons changing coordination environment.

the valence band, forming an isolated band (Figure 6b). Consequently, only the As-p orbitals contribute to the B–As  $\sigma$ bonds. Thus, the s<sup>2</sup> electrons in the s<sup>2</sup>p<sup>3</sup> valence configuration of the As atom do not participate in the bonding and thus form a lone-pair around the As atoms. To have an intuitive view on the lone-pair As-s electrons, we plot the electron localization function (ELF) in Figure 7. The ELF displays the location and size of bonding and lone-pair electrons, which is powerful in interpreting chemical bonding patterns.<sup>34</sup> The ELF values range from 0 to 1, where 0 means no electrons, 0.5 corresponds to the electron-gas-like pair probability, and 1 corresponds to perfect localization. It is well-known that in graphene the C-C  $\sigma$  bonds are contributed from the hybridized C-s/ $p_x/p_y$  orbitals and the solo C- $p_z$  orbital forms the  $\pi$  bonds and the electronic Dirac cone (Figure S3).<sup>37</sup> Thus, there are no lone-pair electrons formed in graphene. By comparing the side views of the ELF between g-BAs (Figure 7b) and graphene (Figure 7a), it can be clearly seen that there are lone-pair electrons localized around As atoms.

It was proposed that lone-pair electrons could lead to low  $\kappa$ . The principle underlying the concept is that the overlapping wave functions of lone-pair electrons with valence (bonding) electrons from adjacent atoms would induce nonlinear electrostatic forces upon thermal agitation, leading to increased phonon anharmonicity in the lattice and thus reducing the  $\kappa$ . 38-45 Due to the orbital distribution in the same energy range and wave functions overlap, as shown in Figures 6a-c and 7b, the nonbonding lone-pair As-s electrons interact with the covalently bonding electrons of adjacent B atoms in g-BAs. The interactions induce a nonlinear electrostatic force among atoms when they thermally vibrate around the equilibrium positions. 46 The nonlinear electrostatic force originates from the asymmetric change of the hybridization between As-s and B-s/p for the atomic motion, as revealed by the pDOS evolution with atom movement (Figure S4). A more asymmetric potential energy well is induced together with the additional nonlinear electrostatic force (Figure 5b), which leads to the strong phonon anharmonicity in g-BAs (Figure 5a) and significantly reduces the  $\kappa$  of g-BAs (Figure 2c).

The form of orbital hybridizations in *c*-BAs is highly consistent with those in *g*-BAs, as shown in Figure 6, which means that lone-pair As-s electrons also emerge around As atoms in *c*-BAs. However, no strong phonon anharmonicity is induced in *c*-BAs by the lone-pair As-s electrons despite the similar orbital hybridization form as *g*-BAs, which is due to the different bonding nature and coordination environment between 3D and 2D geometry structures. Due to the perfect

octahedral coordination of As atoms in *c*-BAs resulting from its cubic structure (Figure 2b), four equivalent valence bonds are formed. Thus, the lone-pair electrons in *c*-BAs are stereochemically inactive despite the interactions with bonding electrons, which has a negligible effect on the phonon anharmonicity. In contrast, for *g*-BAs possessing a planar structure, no pyramidal geometry is formed for the B–As bonds. Consequently, lone-pair As-s electrons are located at both sides of the 2D structure plane in *g*-BAs (Figure 7b), which is different from that in 3D bulk systems of *c*-BAs. Thus, strong phonon anharmonicity exists in *g*-BAs due to the stereochemical activity of the lone-pair As-s electrons in the geometric form of the planar structure.

It is shown in Figure 8 that bond nanodesigning by changing the coordination environment is an effective approach for realizing low  $\kappa$ , which would benefit the design of thermoelectric devices with improved performance. The approaches can also be applied to other materials beyond the BAs systems studied here, for instance, the class of group III-V compounds (e.g., BN, AlN, GaN, etc.), where lone-pair electrons also exist (Figure 1). Strong phonon anharmonicity and low  $\kappa$  could be achieved with the stereochemically activated lone-pair electrons, which can be realized by breaking the perfect octahedral coordination (Figure 2a,b). Note that the 2D structures of the systems presented in Figure 1 and Figure S5 are all planar except for silicene. For the systems with buckled structures in 2D form, such as silicon vs silicene, the situation will be different due to the broken-symmetry-based selection rule for phonon-phonon scattering. 27,29,47 It is found that there exists a strong correlation between the electronegativity difference and the  $\kappa$  modulation for binary compounds (Figure 1). The effect of  $\kappa$  modulation by stereochemically activating the lone-pair electrons is weaker with a larger electronegativity difference. The reason may lie in the contribution to phonon anharmonicity of the electronegativity difference.<sup>27</sup> Other approaches could also have the same effects on the  $\kappa$ modulation that make the lone-pair electrons stereochemically active, such as nanostructuring. Alternatively, it would also be possible by substituting the atoms in ordinary materials with special atoms that can form nonbonding lone-pair electrons, such as nitrogen, phosphorus, arsenic, etc.

Note that the  $\kappa$  of the studied systems here does not achieve an ultralow value, which may limit the direct applications in thermoelectrics. However, if the approach of activating lone-pair electrons is combined with the commonly used strategy of nanostructuring, ultralow  $\kappa$  desirable for thermoelectrics could be effectively achieved. For example, experimental measure-

ments have already demonstrated that the  $\kappa$  of BAs can be suppressed by the arsenic deficiency or vacancy in the BAs sample <sup>12</sup> and the phonon-boundary scattering in BAs microstructures. <sup>13,14</sup> However, the obtained  $\kappa$  of BAs is still too high, which limits its potential applications in thermoelectrics, despite its quite large Seebeck coefficient and thermoelectric power factor. <sup>14</sup> If the lone-pair electrons in the BAs system can be stereochemically activated, the  $\kappa$  could be further reduced, which would improve the thermoelectric performance in the experimental setup. Besides, due to the intrinsic high  $\kappa$ , BAs also shows promising applications in efficient heat dissipation of electronics. When incorporating it into conventional semiconducting devices for heat dissipation, special attention should be paid to avoid activating the lone-pair electrons in BAs-based nanostructures for keeping the high  $\kappa$ .

In summary, by cutting the 3D cubic structure of c-BAs at the (111) cross section, more than 1 order of magnitude lowered  $\kappa$  is achieved in the resultant 2D system of g-BAs with a similar structure as graphene, which shows that bond nanodesigning by transforming the materials into nanoscale with the broken coordination environment could be an effective approach for realizing low  $\kappa$ . Based on the systematic study on the thermal transport properties of g-BAs comparing with c-BAs, diamond, and graphene (c-BAs  $\rightarrow$  g-BAs vs diamond → graphene), the underlying mechanism for the substantially lowered  $\kappa$  in the case of "c-BAs" lies in two aspects: (1) Resulting from the mass difference and 2D nature of bonding and structural symmetry, the weakened bunching effect for acoustic phonon branches together with their coupling with the ZO phonon branch plays a key role in driving the large probability of phonon-phonon scattering. (2) Strong phonon anharmonicity is fundamentally driven by the stereochemically activated lone-pair electrons in g-BAs. Due to the special orbital hybridization, the s<sup>2</sup> electrons in the s<sup>2</sup>p<sup>3</sup> valence configuration of the As atom do not participate in the bonding but form a lone-pair instead. When transforming from the 3D cubic structure of c-BAs to the 2D planar structure of g-BAs, the lone-pair As-s electrons become stereochemically activated due to the break of the perfect octahedral coordination of As atoms in c-BAs, which leads to strong phonon anharmonicity in g-BAs. A similar concept can also be extended to other systems with lone-pair electrons beyond BAs, such as group III-V compounds (e.g., BN, AlN, GaN, etc.), where a strong correlation between  $\kappa$  modulation and electronegativity difference for binary compounds is found. Thus, the lone-pair electrons combined with a small electronegativity difference could be the indicator of lowering  $\kappa$ through bond nanodesigning to change the coordination environment. The proposed approach for realizing low  $\kappa$  and the underlying mechanism uncovered in this study would shed light on future research involving novel materials for energy applications.

#### ■ COMPUTATIONAL DETAILS

All the first-principles calculations are performed based on the density functional theory (DFT) as implemented in the Vienna ab initio simulation package (VASP). The Perdew—Burke—Ernzerhof (PBE) of generalized gradient approximation (GGA) is chosen as the exchange-correlation functional for describing boron arsenide (BAs) systems, which is produced using the projector augmented wave (PAW) method. Based on a careful convergence test, the kinetic energy cutoff of the wave function is set as 800 eV for all the DFT calculations. For

the 2D systems, a large vacuum spacing is necessary to hinder the interactions arising from the employed periodic boundary conditions, which is set as 20 Å along the *out-of-plane* direction. The Monkhorst–Pack  $^{51}$  k-meshes of 15  $\times$  15  $\times$  1 and 2  $\times$  2  $\times$  1 are used to sample the Brillouin zone (BZ) for the structure optimizations and supercell force calculations, respectively, with the energy convergence threshold set as  $10^{-8}$  eV. The structure optimization is fully conducted with no limitation until the maximal Hellmann–Feynman force acting on each atom is less than  $10^{-9}$  eV/Å.

For the supercell force calculations to obtain interatomic force constants (IFCs), a  $5 \times 5 \times 1$  supercell is constructed based on the convergence of the phonon dispersion with respect to the supercell size. The cutoff radius  $(r^{\text{cutoff}})$ introduced during the calculations of the anharmonic IFCs is also fully tested, which is used to discard the interactions between atoms with a distance larger than a certain value for practical purposes. The r cutoff of 10th nearest neighbors (~0.94 nm) is found to be large enough to obtain converged and reliable  $\kappa$ . <sup>52</sup> The space group symmetry properties are used to reduce the computational cost, and the translational and rotational invariance of IFCs are enforced using the Lagrange multiplier method. 53-55 With the anharmonic IFCs, the scattering matrix can be constructed, based on which one can calculate all the three-phonon scattering rates and then obtain the phonon lifetime. The Born effective charge  $(Z^*)$ and dielectric constant  $(\varepsilon)$  obtained based on the density functional perturbation theory (DFPT) are included for taking into account the long-range electrostatic interactions. The thickness for calculating  $\kappa$  is chosen as the van der Waals diameter (3.7 Å). The  $\kappa$  is obtained by solving the linearized phonon BTE using an iterative procedure as implemented in the ShengBTE package based on the IFCs. 55,56 More information can be found in Note S1.

#### ASSOCIATED CONTENT

#### **Data Availability Statement**

The data that support the findings of this study are available from the corresponding author upon request.

#### **Solution** Supporting Information

The Supporting Information is available free of charge at https://pubs.acs.org/doi/10.1021/acs.jpclett.2c03255.

Supplemental table for the specific  $\kappa$  of the typical systems in 3D and 2D forms; supplemental figures for (1) the phonon dispersion showing quadratic behavior of FA, (2) phonon–phonon scattering channels of FA, (3) orbital projected electronic structures for graphene, (4) pDOS evolution for g-BAs due to atomic motion, and (5) normalized  $\kappa$  for several typical 2D materials; and supplemental notes for (1) more details on computational methods and (2) phonon–phonon scattering channels (PDF)

Transparent Peer Review report available (PDF)

#### AUTHOR INFORMATION

#### **Corresponding Authors**

Guangzhao Qin — State Key Laboratory of Advanced Design and Manufacturing for Vehicle Body, College of Mechanical and Vehicle Engineering, Hunan University, Changsha 410082, P. R. China; orcid.org/0000-0001-6770-1096; Email: gzqin@hnu.edu.cn

- Huimin Wang Hunan Key Laboratory for Micro-Nano Energy Materials & Device and School of Physics and Optoelectronics, Xiangtan University, Xiangtan 411105 Hunan, China; Email: wanghmin@xtu.edu.cn
- Zhenzhen Qin School of Physics and Microelectronics, Zhengzhou University, Zhengzhou 450001, China; Email: qzz@zzu.edu.cn
- Ming Hu − Department of Mechanical Engineering, University of South Carolina, Columbia, South Carolina 29208, United States; orcid.org/0000-0002-8209-0139; Email: hu@sc.edu

#### **Author**

Jianhua Xu − State Key Laboratory of Advanced Design and Manufacturing for Vehicle Body, College of Mechanical and Vehicle Engineering, Hunan University, Changsha 410082, P. R. China; orcid.org/0000-0003-2294-8815

Complete contact information is available at: https://pubs.acs.org/10.1021/acs.jpclett.2c03255

#### Notes

The authors declare no competing financial interest.

#### ACKNOWLEDGMENTS

G.Q. is supported by the National Natural Science Foundation of China (Grant No. 52006057), the Fundamental Research Funds for the Central Universities (Grant Nos. 531119200237 and 541109010001), and the State Key Laboratory of Advanced Design and Manufacturing for Vehicle Body at Hunan University (Grant No. 52175013). H.W. is supported by the National Natural Science Foundation of China (Grant No. 51906097). Z.Q. is supported by the National Natural Science Foundation of China (Grant No. 11904324, 12274374), the Natural Science Foundation of Henan Province of China (Grant No. 222300420551). M.H. is supported by the NSF (Grant No. 2030128). Simulations were performed with computing resources granted by RWTH Aachen University under projects rwth0366. The numerical calculations in this paper have also been done on the supercomputing system of the E.T. Cluster and the National Supercomputing Center in Changsha.

#### REFERENCES

- (1) Biswas, K.; He, J.; Blum, I. D.; Wu, C.-I.; Hogan, T. P.; Seidman, D. N.; Dravid, V. P.; Kanatzidis, M. G. High-Performance Bulk Thermoelectrics with All-Scale Hierarchical Architectures. *Nature* **2012**, *489* (7416), 414–418.
- (2) Qin, G.; Yan, Q.-B.; Qin, Z.; Yue, S.-Y.; Cui, H.-J.; Zheng, Q.-R.; Su, G. Hinge-like Structure Induced Unusual Properties of Black Phosphorus and New Strategies to Improve the Thermoelectric Performance. *Sci. Rep* **2014**, *4* (1), 6946.
- (3) Zhao, L.-D.; Tan, G.; Hao, S.; He, J.; Pei, Y.; Chi, H.; Wang, H.; Gong, S.; Xu, H.; Dravid, V. P.; Uher, C.; Snyder, G. J.; Wolverton, C.; Kanatzidis, M. G. Ultrahigh Power Factor and Thermoelectric Performance in Hole-Doped Single-Crystal SnSe. *Science* **2016**, *351* (6269), 141–144.
- (4) Zhang, X.; Xie, H.; Hu, M.; Bao, H.; Yue, S.; Qin, G.; Su, G. Thermal Conductivity of Silicene Calculated Using an Optimized Stillinger-Weber Potential. *Phys. Rev. B* **2014**, *89* (5), 054310.
- (5) Shin, J.; Gamage, G. A.; Ding, Z.; Chen, K.; Tian, F.; Qian, X.; Zhou, J.; Lee, H.; Zhou, J.; Shi, L.; Nguyen, T.; Han, F.; Li, M.; Broido, D.; Schmidt, A.; Ren, Z.; Chen, G. High Ambipolar Mobility in Cubic Boron Arsenide. *Science* **2022**, *377* (6604), 437–440.

- (6) Lindsay, L.; Broido, D. A.; Reinecke, T. L. First-Principles Determination of Ultrahigh Thermal Conductivity of Boron Arsenide: A Competitor for Diamond? *Phys. Rev. Lett.* **2013**, *111* (2), 025901.
- (7) Ma, H.; Li, C.; Tang, S.; Yan, J.; Alatas, A.; Lindsay, L.; Sales, B. C.; Tian, Z. Boron Arsenide Phonon Dispersion from Inelastic X-Ray Scattering: Potential for Ultrahigh Thermal Conductivity. *Phys. Rev. B* **2016**, 94 (22), 220303.
- (8) Feng, T.; Lindsay, L.; Ruan, X. Four-Phonon Scattering Significantly Reduces Intrinsic Thermal Conductivity of Solids. *Phys. Rev. B* **2017**, *96* (16), 161201.
- (9) Kang, J. S.; Li, M.; Wu, H.; Nguyen, H.; Hu, Y. Experimental Observation of High Thermal Conductivity in Boron Arsenide. *Science* **2018**, *361* (6402), 575–578.
- (10) Li, S.; Zheng, Q.; Lv, Y.; Liu, X.; Wang, X.; Huang, P. Y.; Cahill, D. G.; Lv, B. High Thermal Conductivity in Cubic Boron Arsenide Crystals. *Science* **2018**, *361* (6402), 579–581.
- (11) Tian, F.; Song, B.; Chen, X.; Ravichandran, N. K.; Lv, Y.; Chen, K.; Sullivan, S.; Kim, J.; Zhou, Y.; Liu, T.-H.; Goni, M.; Ding, Z.; Sun, J.; Udalamatta Gamage, G. A. G.; Sun, H.; Ziyaee, H.; Huyan, S.; Deng, L.; Zhou, J.; Schmidt, A. J.; Chen, S.; Chu, C.-W.; Huang, P. Y.; Broido, D.; Shi, L.; Chen, G.; Ren, Z. Unusual High Thermal Conductivity in Boron Arsenide Bulk Crystals. *Science* **2018**, *361* (6402), 582–585.
- (12) Lv, B.; Lan, Y.; Wang, X.; Zhang, Q.; Hu, Y.; Jacobson, A. J.; Broido, D.; Chen, G.; Ren, Z.; Chu, C.-W. Experimental Study of the Proposed Super-Thermal-Conductor: BAs. *Appl. Phys. Lett.* **2015**, *106* (7), 074105.
- (13) Broido, D. A.; Lindsay, L.; Reinecke, T. L. Ab Initio Study of the Unusual Thermal Transport Properties of Boron Arsenide and Related Materials. *Phys. Rev. B* **2013**, *88* (21), 214303.
- (14) Kim, J.; Evans, D. A.; Sellan, D. P.; Williams, O. M.; Ou, E.; Cowley, A. H.; Shi, L. Thermal and Thermoelectric Transport Measurements of an Individual Boron Arsenide Microstructure. *Appl. Phys. Lett.* **2016**, *108* (20), 201905.
- (15) Mohanta, M. K.; Dimple; Rawat, A.; Jena, N.; Ahammed, R.; De Sarkar, A. Ultra-Low Thermal Conductivity and Super-Slow Hot-Carrier Thermalization Induced by a Huge Phononic Gap in Multifunctional Nanoscale Boron Pnictides. *Physica E: Low-dimensional Systems and Nanostructures* **2020**, *124*, 114222.
- (16) Shi, J.; Han, C.; Wang, X.; Yun, S. Electronic, Elastic and Piezoelectric Properties of Boron-V Group Binary and Ternary Monolayers. *Physica B: Condensed Matter* **2019**, *574*, 311634.
- (17) Manoharan, K.; Subramanian, V. Exploring Multifunctional Applications of Hexagonal Boron Arsenide Sheet: A DFT Study. *ACS Omega* **2018**, *3* (8), 9533–9543.
- (18) Xie, M.; Cai, B.; Meng, Z.; Gu, Y.; Zhang, S.; Liu, X.; gong, L.; Li, X.; Zeng, H. Two-Dimensional BAs/InTe: A Promising Tandem Solar Cell with High Power Conversion Efficiency. ACS Appl. Mater. Interfaces 2020, 12 (5), 6074–6081.
- (19) Zhang, R.; Zhang, C.; Ji, W.; Li, S.; Wang, P.; Hu, S.; Yan, S. Hydrogenated Boron Arsenide Nanosheet: A Promising Candidate for Bipolar Magnetic Semiconductor. *Appl. Phys. Express* **2015**, 8 (11), 113001.
- (20) Hoat, D. M.; Naseri, M.; Hieu, N. N.; Ponce-Pérez, R.; Tong, H. D.; Rivas-Silva, J. F.; Vu, T. V.; Cocoletzi, G. H. Half-Metallicity and Magnetism in BAs Monolayer Induced by Anchoring 3d Transition Metals (TM = V, Cr and Mn). Superlattices Microstruct. 2020, 139, 106399.
- (21) Camacho-Mojica, D. C.; López-Urías, F. Design of BAs-AlN Monolayered Honeycomb Heterojunction Structures: A First-Principles Study. *Appl. Surf. Sci.* **2016**, *368*, 191–197.
- (22) Attia, A. A.; Jappor, H. R. Tunable Electronic and Optical Properties of New Two-Dimensional GaN/BAs van Der Waals Heterostructures with the Potential for Photovoltaic Applications. *Chem. Phys. Lett.* **2019**, 728, 124–131.
- (23) Kanwal, A.; Jalil, A.; Ilyas, S. Z.; Ahmed, S.; Agathopoulos, S.; Znaidia, S. Effect of Electric Field on Two-Dimensional Honeycomb Structures from Group (III–V). *J. Phys. Chem. Solids* **2022**, *162*, 110507.

- (24) Raeisi, M.; Ahmadi, S.; Rajabpour, A. Modulated Thermal Conductivity of 2D Hexagonal Boron Arsenide: A Strain Engineering Study. *Nanoscale* **2019**, *11* (45), 21799–21810.
- (25) Fan, H.; Wu, H.; Lindsay, L.; Hu, Y. Ab Initio Investigation of Single-Layer High Thermal Conductivity Boron Compounds. *Phys. Rev. B* **2019**, *100* (8), 085420.
- (26) Hu, Y.; Li, D.; Yin, Y.; Li, S.; Zhou, H.; Zhang, G. High Thermal Conductivity Driven by the Unusual Phonon Relaxation Time Platform in 2D Monolayer Boron Arsenide. *RSC Adv.* **2020**, *10* (42), 25305–25310.
- (27) Qin, Z.; Qin, G.; Zuo, X.; Xiong, Z.; Hu, M. Orbitally Driven Low Thermal Conductivity of Monolayer Gallium Nitride (GaN) with Planar Honeycomb Structure: A Comparative Study. *Nanoscale* **2017**, *9* (12), 4295–4309.
- (28) Greene, R. G.; Luo, H.; Ruoff, A. L.; Trail, S. S.; DiSalvo, F. J. Pressure Induced Metastable Amorphization of BAs: Evidence for a Kinetically Frustrated Phase Transformation. *Phys. Rev. Lett.* **1994**, 73 (18), 2476–2479.
- (29) Qin, G.; Qin, Z.; Wang, H.; Hu, M. Anomalously Temperature-Dependent Thermal Conductivity of Monolayer GaN with Large Deviations from the Traditional 1/T Law. *Phys. Rev. B* **2017**, *95* (19), 195416.
- (30) Ward, A.; Broido, D. A. Intrinsic Phonon Relaxation Times from First-Principles Studies of the Thermal Conductivities of Si and Ge. *Phys. Rev. B* **2010**, *81* (8), 085205.
- (31) Ward, A.; Broido, D. A.; Stewart, D. A.; Deinzer, G. Ab Initio Theory of the Lattice Thermal Conductivity in Diamond. *Phys. Rev. B* **2009**, *80* (12), 125203.
- (32) Omini, M.; Sparavigna, A. Beyond the Isotropic-Model Approximation in the Theory of Thermal Conductivity. *Phys. Rev. B* **1996**, 53 (14), 9064–9073.
- (33) Lindsay, L.; Broido, D. A. Three-Phonon Phase Space and Lattice Thermal Conductivity in Semiconductors. *J. Phys.: Condens. Matter* **2008**, *20* (16), 165209.
- (34) Qin, G.; Zhang, X.; Yue, S.-Y.; Qin, Z.; Wang, H.; Han, Y.; Hu, M. Resonant Bonding Driven Giant Phonon Anharmonicity and Low Thermal Conductivity of Phosphorene. *Phys. Rev. B* **2016**, *94* (16), 165445.
- (35) Zeier, W. G.; Zevalkink, A.; Gibbs, Z. M.; Hautier, G.; Kanatzidis, M. G.; Snyder, G. J. Thinking Like a Chemist: Intuition in Thermoelectric Materials. *Angew. Chem., Int. Ed.* **2016**, *55* (24), 6826–6841.
- (36) Zhao, L.-D.; Chang, C.; Tan, G.; Kanatzidis, M. G. SnSe: A Remarkable New Thermoelectric Material. *Energy Environ. Sci.* **2016**, 9 (10), 3044–3060.
- (37) Balandin, A. A.; Nika, D. L. Phononics in Low-Dimensional Materials. *Mater. Today* **2012**, *15* (6), 266–275.
- (38) Petrov, A. V.; Shtrum, E. L. Heat Conductivity and The Chemical Born in ABX<sub>2</sub>-Type Compounds. *Sov. Phys. Solid State* **1962**, *4* (6), 1061–1065.
- (39) Morelli, D. T.; Jovovic, V.; Heremans, J. P. Intrinsically Minimal Thermal Conductivity in Cubic I-V-VI<sub>2</sub> Semiconductors. *Phys. Rev. Lett.* **2008**, *101* (3), 035901.
- (40) Skoug, E. J.; Morelli, D. T. Role of Lone-Pair Electrons in Producing Minimum Thermal Conductivity in Nitrogen-Group Chalcogenide Compounds. *Phys. Rev. Lett.* **2011**, *107* (23), 235901.
- (41) Nielsen, M. D.; Ozolins, V.; Heremans, J. P. Lone Pair Electrons Minimize Lattice Thermal Conductivity. *Energy Environ. Sci.* **2013**, *6* (2), 570–578.
- (42) Heremans, J. P. The Anharmonicity Blacksmith. *Nature Phys.* **2015**, *11* (12), 990–991.
- (43) Jana, M. K.; Pal, K.; Waghmare, U. V.; Biswas, K. The Origin of Ultralow Thermal Conductivity in InTe: Lone-Pair-Induced Anharmonic Rattling. *Angew. Chem., Int. Ed.* **2016**, *55* (27), *7792*–*7796*.
- (44) Xiao, Y.; Chang, C.; Pei, Y.; Wu, D.; Peng, K.; Zhou, X.; Gong, S.; He, J.; Zhang, Y.; Zeng, Z.; Zhao, L.-D. Origin of Low Thermal Conductivity in SnSe. *Phys. Rev. B* **2016**, 94 (12), 125203.
- (45) Yu, L.-F.; Xu, J.-Y.; Shen, C.; Zhou, E.; Wu, J.; Zhang, H.-B.; Zheng, X.; Wang, H.-M.; Qin, G.-Z. Realizing Ultra-Low Thermal

- Conductivity by Strong Synergy of Asymmetric Geometry and Electronic Structure in Boron Nitride and Arsenide. *Rare Metals* **2023**, 42, 210.
- (46) Qin, G.; Qin, Z.; Wang, H.; Hu, M. Lone-Pair Electrons Induced Anomalous Enhancement of Thermal Transport in Strained Planar Two-Dimensional Materials. *Nano Energy* **2018**, *50*, 425–430.
- (47) Lindsay, L.; Broido, D. A.; Mingo, N. Flexural Phonons and Thermal Transport in Graphene. *Phys. Rev. B* **2010**, 82 (11), 115427.
- (48) Kresse, G.; Furthmüller, J. Efficient Iterative Schemes for Ab Initio Total-Energy Calculations Using a Plane-Wave Basis Set. *Phys. Rev. B* **1996**, 54 (16), 11169–11186.
- (49) Perdew, J. P.; Burke, K.; Ernzerhof, M. Generalized Gradient Approximation Made Simple. *Phys. Rev. Lett.* **1996**, 77 (18), 3865–3868
- (50) Kresse, G.; Joubert, D. From Ultrasoft Pseudopotentials to the Projector Augmented-Wave Method. *Phys. Rev. B* **1999**, *59* (3), 1758–1775.
- (51) Monkhorst, H. J.; Pack, J. D. Special Points for Brillouin-Zone Integrations. *Phys. Rev. B* **1976**, *13* (12), 5188–5192.
- (52) Qin, G.; Hu, M. Accelerating Evaluation of Converged Lattice Thermal Conductivity. *npj Comput. Mater.* **2018**, *4* (1), 3.
- (53) Togo, A.; Oba, F.; Tanaka, I. First-Principles Calculations of the Ferroelastic Transition between Rutile-Type and CaCl<sub>2</sub>-Type SiO<sub>2</sub> at High Pressures. *Phys. Rev. B* **2008**, 78 (13), 134106.
- (54) Esfarjani, K.; Stokes, H. T. Method to Extract Anharmonic Force Constants from First Principles Calculations. *Phys. Rev. B* **2008**, 77 (14), 144112.
- (55) Li, W.; Lindsay, L.; Broido, D. A.; Stewart, D. A.; Mingo, N. Thermal Conductivity of Bulk and Nanowire Mg<sub>2</sub>Si<sub>x</sub>Sn<sub>1-x</sub> Alloys from First Principles. *Phys. Rev. B* **2012**, *86* (17), 174307.
- (56) Li, W.; Carrete, J.; Katcho, N. A.; Mingo, N. ShengBTE: A Solver of the Boltzmann Transport Equation for Phonons. *Comput. Phys. Commun.* **2014**, *185* (6), 1747–1758.

### **□** Recommended by ACS

## Reducing the $\beta\text{-}Ga_2O_3$ Epitaxy Temperature to 240 °C via Atomic Layer Plasma Processing

Saidjafarzoda Ilhom, Necmi Biyikli, et al.

DECEMBER 27, 2022

ACS APPLIED ELECTRONIC MATERIALS

READ 🗹

#### **Efficient n-Type Surface Doping in Diamond**

Yaning Liu, Hongdong Li, et al.

DECEMBER 28, 2022

THE JOURNAL OF PHYSICAL CHEMISTRY C

READ 🗹

### Edge-Active Enriched MoS<sub>2</sub> Porous Nanosheets as Efficient Pt-Free Catalysts toward the Triiodide Reduction Reaction

Yuying Cao, Bing Zhao, et al.

DECEMBER 29, 2022

ACS APPLIED ELECTRONIC MATERIALS

READ 🗹

### Elucidating $NO_x$ Surface Chemistry at the Anatase (101) Surface in $TiO_2$ Nanoparticles

Lorenzo Mino, Michele Ceotto, et al.

DECEMBER 28, 2022

THE JOURNAL OF PHYSICAL CHEMISTRY C

READ 🗹

Get More Suggestions >